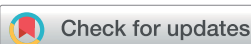


## EDGE ARTICLE

Cite this: *Chem. Sci.*, 2021, **12**, 688 All publication charges for this article have been paid for by the Royal Society of Chemistry

## Structural insight into [Fe–S<sub>2</sub>–Mo] motif in electrochemical reduction of N<sub>2</sub> over Fe<sub>1</sub>-supported molecular MoS<sub>2</sub>†

Jianwei Zheng,<sup>a</sup> Simson Wu,<sup>a</sup> Lilin Lu,<sup>b</sup> Chen Huang,<sup>c</sup> Ping-Luen Ho,<sup>a</sup> Angus Kirkland,<sup>c</sup> Tim Sudmeier,<sup>a</sup> Rosa Arrigo,<sup>de</sup> Diego Gianolio<sup>d</sup> and Shik Chi Edman Tsang<sup>a</sup> 

The catalytic synthesis of NH<sub>3</sub> from the thermodynamically challenging N<sub>2</sub> reduction reaction under mild conditions is currently a significant problem for scientists. Accordingly, herein, we report the development of a nitrogenase-inspired inorganic-based chalcogenide system for the efficient electrochemical conversion of N<sub>2</sub> to NH<sub>3</sub>, which is comprised of the basic structure of [Fe–S<sub>2</sub>–Mo]. This material showed high activity of 8.7 mg<sub>NH<sub>3</sub></sub> mg<sub>Fe</sub><sup>-1</sup> h<sup>-1</sup> (24 μg<sub>NH<sub>3</sub></sub> cm<sup>-2</sup> h<sup>-1</sup>) with an excellent faradaic efficiency of 27% for the conversion of N<sub>2</sub> to NH<sub>3</sub> in aqueous medium. It was demonstrated that the Fe<sub>1</sub> single atom on [Fe–S<sub>2</sub>–Mo] under the optimal negative potential favors the reduction of N<sub>2</sub> to NH<sub>3</sub> over the competitive proton reduction to H<sub>2</sub>. *Operando* X-ray absorption and simulations combined with theoretical DFT calculations provided the first and important insights on the particular electron-mediating and catalytic roles of the [Fe–S<sub>2</sub>–Mo] motifs and Fe<sub>1</sub>, respectively, on this two-dimensional (2D) molecular layer slab.

Received 20th August 2020  
Accepted 21st October 2020DOI: 10.1039/d0sc04575f  
[rsc.li/chemical-science](http://rsc.li/chemical-science)

## Introduction

NH<sub>3</sub> is a chemical that can be used as a fertilizer and carbon-free energy store. The industrial production of NH<sub>3</sub> from N<sub>2</sub> and hydrogen (H<sub>2</sub>) *via* the Haber Bosch (HB) process is well developed, but simultaneously, it is very energy demanding and environmentally unfriendly.<sup>1,2</sup> The HB process is normally conducted at high pressure and high temperature (400–500 °C and 100–200 bar, respectively), which accounts for 1–2% of the global annual energy output.<sup>3,4</sup> This is due to the difficulty in this reaction route to dissociate the strong N≡N triple bond of N<sub>2</sub> for the production of ammonia.<sup>5</sup> In addition, H<sub>2</sub> as a reactant for the HB process is predominately derived from fossil fuel, which is responsible for about 1% of the global greenhouse gas emission.<sup>2</sup> Thus, several new attempts have been developed to replace the HB process using renewable energies. For example, decentralized pilot plants have been built to convert solar, wind, and tidal power to H<sub>2</sub> *via* renewable electricity for the synthesis

of NH<sub>3</sub> (eHB) (see Fig. S1†).<sup>6,7</sup> Furthermore, as a potential new process, it is even more attractive to produce NH<sub>3</sub> directly from the electrochemical reaction of N<sub>2</sub> and H<sub>2</sub>O under ambient conditions. However, this still has to be developed using more effective catalysts.<sup>8</sup>

For low-temperature N<sub>2</sub> catalytic fixation to NH<sub>3</sub>, the associative mechanism most likely occurs through enzymatic, photo- or electro-chemical means.<sup>9–11</sup> For these processes, N<sub>2</sub> fixation through enzyme nitrogenase is the most efficient route to produce NH<sub>3</sub>, which has also been adopted in nature. Thus, substantial efforts have been devoted to understanding and mimicking how the nitrogenase enzyme accomplishes the reduction of N<sub>2</sub> at ambient temperature and pressure.<sup>12,13</sup> Many homogeneous catalysts act as well-defined molecular systems to provide important mechanistic insights.<sup>14–16</sup> On the other hand, inorganic-based nitrogenase mimics can potentially accomplish N<sub>2</sub> fixation and convert it into NH<sub>3</sub> under ambient conditions with light or electricity input.<sup>10,11,17,18</sup> For example, heterogeneous catalysts in the form of transition metal chalcogenides, including Mo- and Fe-containing sulphide clusters, have been reported to catalyze the reduction of N<sub>2</sub> to NH<sub>3</sub>.<sup>17,18</sup> However, these structures are not well-defined and cannot provide as much mechanistic guidance as that of the homogeneous catalysts.

In addition, a number of these solid electrocatalysts suffer from slow kinetics due to the low N<sub>2</sub> reduction. Also, H<sub>2</sub> from competitive proton (water) reduction occurs over the same active sites.<sup>8</sup> It has been reported that proton reduction is

<sup>a</sup>Wolfson Catalysis Centre, Department of Chemistry University of Oxford, Oxford, OX1 3QR, UK. E-mail: edman.tsang@chem.ox.ac.uk

<sup>b</sup>College of Chemistry and Chemical Engineering, Wuhan University of Science and Technology, China

<sup>c</sup>Department of Materials, University of Oxford, Oxford, OX1 PH, UK

<sup>d</sup>Diamond Light Source, Harwell Campus, Chilton, Oxfordshire OX11 0DE, UK

<sup>e</sup>School of Science, Engineering and Environment, University of Salford, Manchester, M5 4WT, UK

† Electronic supplementary information (ESI) available. See DOI: [10.1039/d0sc04575f](https://doi.org/10.1039/d0sc04575f)



thermodynamically more favorable than  $\text{N}_2$  reduction under negative potentials (see Fig. S2†).<sup>19</sup> The adsorption and reduction of  $\text{H}^+$  to surface  $\text{H}^*$  are potential dependent and can be rate-limiting on a specific catalyst. If this competitive route is suppressed, then it may dramatically enhance the faradaic efficiency ( $\eta_{\text{FE}}$ ) for  $\text{N}_2$  reduction.<sup>20,21</sup> Therefore, the design of inherently active and selective electrocatalysts with a suitable surface for  $\text{N}_2$  reduction relies on controlling the applied potential to attenuate or totally inhibit the  $\text{H}_2$  evolution process, while enhancing the activation of  $\text{N}_2$ . The activity of transition metals for the synthesis of  $\text{NH}_3$  has been rationalized in terms of the  $\text{N}_2$  binding energy by Norskov and co-workers.<sup>22</sup> Their results showed that transition metals with half-electron filled 3d orbitals, such as Ru, Os and Fe, have a relative lower adsorption energy ( $-55\text{--}10 \text{ kJ mol}^{-1}$   $\text{N}_2$ ) for  $\text{N}_2$ , which results in higher turnover frequencies for the synthesis of  $\text{NH}_3$ . As both a non-noble metal and the active ingredient of the nitrogenase enzyme,<sup>23,24</sup> Fe is a potential candidate for the electrochemical synthesis of  $\text{NH}_3$ .

Herein, we developed a structurally well-defined single-atom catalyst consisting of isolated  $\text{Fe}_1$  anchored on exfoliated molecular-layered  $\text{MoS}_2$  for the efficient  $\text{N}_2$  reduction reaction (NRR) to  $\text{NH}_3$  of  $8.7 \text{ mg}_{\text{NH}_3} \text{ mg}_{\text{Fe}}^{-1} \text{ h}^{-1}$  in water under an applied potential, which could also offer a high  $\eta_{\text{FE}}$  of 27% over  $\text{H}_2$  evolution from water electrolysis. It is interesting to find that this single-atom  $\text{Fe}_1$  catalyst possesses similar  $[\text{Fe}-\text{S}_2-\text{Mo}]$  motifs to the core-structure of the  $\text{FeMo}$  sulfur (S) clusters in the nitrogenase enzyme. This makes the single-atom  $\text{Fe}_1$  the catalytic redox active centers, which combined with the electronic-mediating  $[\text{Fe}-\text{S}_2-\text{Mo}]$  units, boost the electrochemical reduction of  $\text{N}_2$  over the  $\text{Fe}_1$  single-atom catalyst was investigated *via* *operando* synchrotron-radiation X-ray absorption fine structure (opXAFS), X-ray absorption near edge structure (XANES) spectroscopy and

density functional theory (DFT) calculations. The mechanistic pathways and structure–activity relationships were deduced over this inorganic nitrogenase mimic  $[\text{Fe}-\text{S}_2-\text{Mo}]$ , providing guiding principles for the NRR.

## Results and discussion

### Structure of $\text{Fe}_1$ single-atom on single-layer $\text{MoS}_2$

The  $\text{MoS}_2$  matrix was firstly treated with *n*-butyllithium solution in hexane<sup>25</sup> to exfoliate bulk  $\text{MoS}_2$  to form 2D mono-layered  $\text{MoS}_2$ . The X-ray diffraction (XRD, Fig. S3†) pattern and atomic force microscopy (AFM, Fig. S4†) image show that around 60% of the exfoliated  $\text{MoS}_2$  is single molecular layers. Subsequently, single-atom  $\text{Fe}_1$  was introduced on the three-sublayer S-Mo-S in trigonal prismatic 2-H structure mono-layered  $\text{MoS}_2$  *via* the hydrothermal method. No peaks corresponding to Fe-based aggregated species were detected in the XRD patterns and TEM images, demonstrating the high dispersion of the  $\text{Fe}_1$  atoms.

The existence of dispersed Fe atoms on the basal plane of  $\text{MoS}_2$  was clearly verified by high-angle annular dark-field scanning transmission electron microscopy (HAADF-STEM), as shown in Fig. 1. Single-layer  $\text{MoS}_2$  nanosheets with a 2H trigonal prismatic symmetry pattern can be clearly seen. For single-atom catalysis, the specific chemical environment of the atom is critical since its coordinated feature can significantly affect its catalytic behavior and performance. For most of the reported supported single-atom (active site) materials, although the atoms could be directly visualized using the recently developed HAADF-STEM technique, their atomic positions with respect to the support structures were not clear and well-defined; hence, obscuring the derivation of the important structure–activity relationships. In contrast, our single-atom Fe on single-molecular layered  $\text{MoS}_2$  (s $\text{MoS}_2$ ) exhibited clear

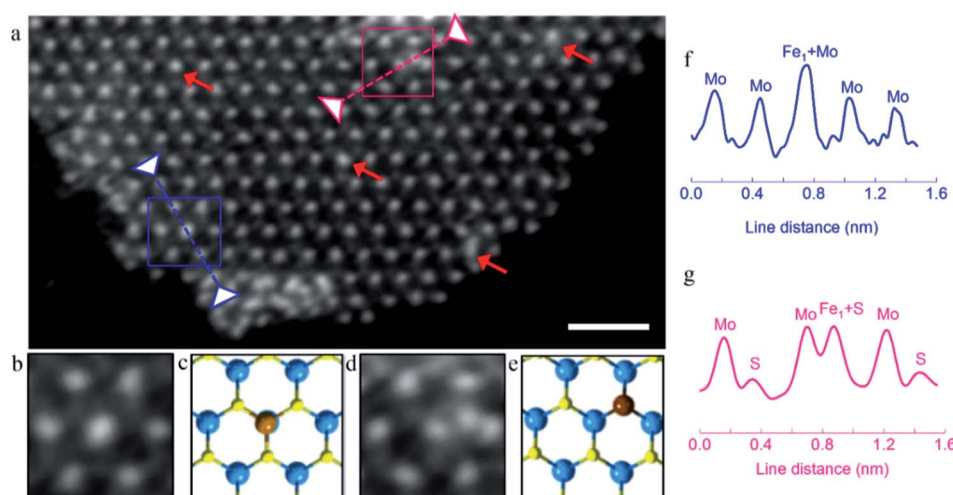


**Fig. 1** Morphology and structural characterization of Fe-s $\text{MoS}_2$ . (a) HAADF-STEM image of Fe-s $\text{MoS}_2$  sheet, scale bar is 1 nm. Chemical environments of  $\text{Fe}_1$  can be seen in the two enlarged square boxes, where Scan 1 (blue line) shows the  $\text{Fe}_1$  atom on the Mo atop site and Scan 2 (pink line) shows the  $\text{Fe}_1$  atom substituted on the S site. The red arrows indicate individual  $\text{Fe}_1$  atoms on the Mo atop site. (b) HAADF-STEM scan, (c) corresponding DFT optimized model and (f) ADF intensity profile analysis of the  $\text{Fe}_1$  atom on the Mo atop site. (d) HAADF-STEM scan, (e) corresponding DFT optimized model and (g) ADF intensity profile analysis of the  $\text{Fe}_1$  atom as the substituted S site.

bonding environments. As shown in Fig. 1, isolated  $\text{Fe}_1$  atoms are located at two types of preferred positions on the basal plane of  $\text{sMoS}_2$ , namely the Mo atop site and substituted S atom site. They were revealed by the brighter spots than the surrounding Mo or S<sub>2</sub> sites in the 2-H arrangement, typically as presented in the blue and pink squares, respectively. Further evidence was obtained from the DFT simulations (Fig. S5†), enlarged HAADF-STEM image, corresponding model and intensity profile analysis, as shown in Fig. 1b, c and f, respectively showing that the  $\text{Fe}_1$  atom sits on the triangle S sites, which is directly on the top position of Mo as the atop site. Similarly, Fig. 1d, e and g show that the Fe atom is located on the S basal site of 2H- $\text{sMoS}_2$ , where the intensity profile suggests that S is substituted by the Fe atom. It should be noted that most of the  $\text{Fe}_1$  single atoms were found on the Mo atop sites, and occasionally on the S substitution sites.

To obtain bonding information on the anchored  $\text{Fe}_1$  atom, experimental XAFS (Fig. 2a) spectra were collected together with DFT simulations. Fig. 2a shows the Fourier transform spectrum of the Fe K-edge XAFS oscillations of the as-reduced Fe- $\text{sMoS}_2$  in comparison with the standard Fe foil. The absence of Fe–Fe interaction in the FT-XAFS spectra indicates the single-atom configuration of  $\text{Fe}_1$ . The peak at approximately 1.7 Å is mainly attributed to the Fe–S bonds at the Mo atop site. The simulation of the structure with the corresponding bonding distance is shown in the inset of Fig. 2a. Wavelet transformed analysis of XAFS (WT-XAFS, Fig. 2c) based on Morlet wavelets was conducted to differentiate the closely-related spatial interactions<sup>26</sup> of the  $\text{Fe}_1$  atoms with their proximal atoms. As displayed in Fig. 2c, the Fe–Fe bonds in the Fe foil show an energy maximum in the range of 7–11 Å<sup>-1</sup>, while that for Fe- $\text{sMoS}_2$  is in

the range of 4–9 Å<sup>-1</sup>. This again supports the fact that the Fe species are individually dispersed as single atoms, as shown by the HADDF-STEM image (Fig. 1), mainly at the Mo atop sites.

The bonding environment of the  $\text{Fe}_1$  atom at the Mo atop site was simulated by DFT, and the result is shown in Fig. S5.† Interestingly, the structure in the model of  $\text{Fe}_1$  at the Mo atop site has almost the same inorganic motif of [Fe–S<sub>2</sub>–Mo] with that of the core structure of FeMoco, the primary cofactor of nitrogenase, giving equivalent bond lengths and geometries of the coordinated  $\text{Fe}_1$  shells (see Table S1†).<sup>24,27</sup> In addition to the similar bonding environment of Fe, according to the XANES analysis, the absorption edge is clearly located between  $\text{Fe}^{\text{II}}$  and  $\text{Fe}^{\text{III}}$ , indicating that the oxidation state of the Fe species in Fe- $\text{sMoS}_2$  is also close to that of the working state of FeMoco,<sup>28</sup> as shown in Fig. 2b. Of particular interest is the characteristic peak below the absorption edge of Fe- $\text{sMoS}_2$ . It is well known that this pre-edge feature is due to the  $1\text{s} \rightarrow 3\text{d}$  orbital forbidden transition, which would be excluded by dipole selection rules for a symmetry site.<sup>29</sup> The observed pre-edge peak matches with the characterized isolated  $\text{Fe}_1$  on  $\text{sMoS}_2$ .

### Electrochemical N<sub>2</sub> reduction

The material was then tested for electrochemical N<sub>2</sub> conversion to NH<sub>3</sub> in water under ambient conditions. The catalyst was deposited on carbon paper as a cathode under a flowing stream of N<sub>2</sub> feed gas. It has been noted in the literature in this field that carefully designed blanks must be employed to confirm the nitrogen reduction reaction activity of any material. For example, it has been reported that contaminants such as NO<sub>x</sub> may also participate in the synthesis of ammonia.<sup>30,31</sup> NaClO<sub>2</sub> is known to be one of the most efficient chemicals for NO<sub>x</sub> oxidation due to its strong oxidation power.<sup>32,33</sup> Thus, to remove the interference of NO<sub>x</sub>, two traps filled with 0.2 M NaClO<sub>2</sub> solution and 1 mM H<sub>2</sub>SO<sub>4</sub> solution were used to purify the feed gas before it was flowed into the three-electrode single cell. The ability to remove NO<sub>x</sub> is evidenced in Fig. S6.† In a previously established N<sub>2</sub> purification protocol, gas cleaning of the filters following by acid trapping were employed to remove NO<sub>x</sub>.<sup>34</sup> The two methods were compared, and the results were within an acceptable deviation of 8.3%. Prior to each test, blank measurements in the absence of N<sub>2</sub> and catalyst were conducted.<sup>35–38</sup> The obtained reaction assay was measured by two independent methods, namely the indophenol blue method (Fig. S7†) and ammonia selective electrode.<sup>39</sup> The detail mechanism of the ammonia selective electrode is presented in the ESI.† The calibration curves are shown in Fig. S8 and S9,† respectively. The results from the two methods were in a good agreement. We firstly optimized the over-potential required for the maximum production of NH<sub>3</sub> over Fe- $\text{sMoS}_2$  in the range of –0.05 V to –1.00 V (*versus* the reversible H<sub>2</sub> electrode (RHE)). As shown in Fig. S10,† the current density increased as the applied potential increased, and was more stable at low potential. The highest rate of NH<sub>3</sub> production was 24.5 μg<sub>NH<sub>3</sub></sub> cm<sup>-2</sup> h<sup>-1</sup> (8.7 mg<sub>NH<sub>3</sub></sub> mg<sub>Fe</sub><sup>-1</sup> h<sup>-1</sup>) at –0.10 V (*versus* RHE, see Fig. 3a) with a maximum η<sub>FE</sub> of ca. 27.0% (Fig. 3b). To the best of our knowledge, this electrocatalytic performance is among the best

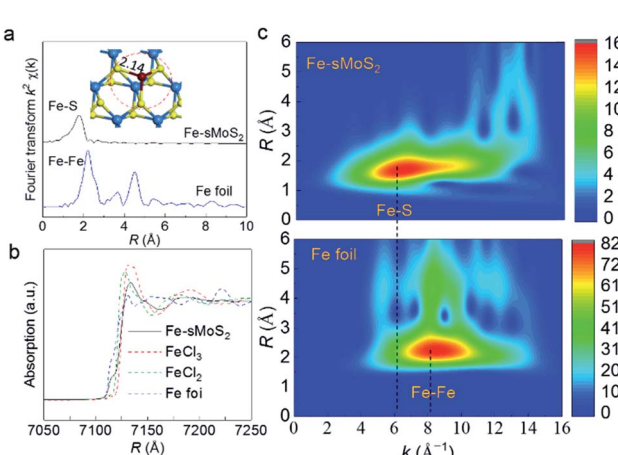
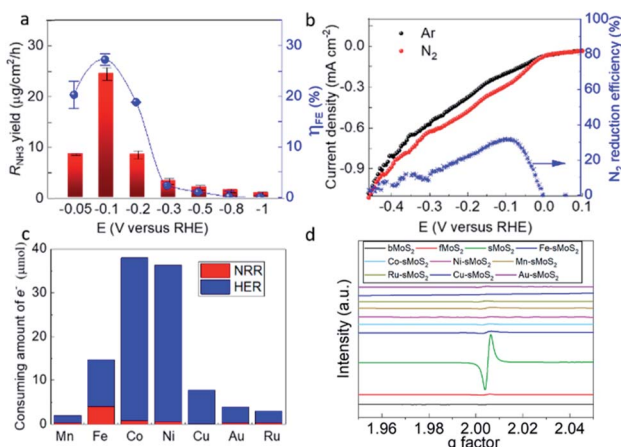


Fig. 2 Bonding environment of  $\text{Fe}_1$  atom in Fe- $\text{sMoS}_2$ . (a) Fourier transform Fe K-edge XAFS spectra of Fe- $\text{sMoS}_2$  with reference to Fe foil. Inset shows the DFT model for  $\text{Fe}_1$  atom at Mo atop site with the peak matching to that expected from the corresponding Fe–S distance and absence of Fe–Fe in both models. (b) Fe K-edge XANES spectra of atomically dispersed Fe- $\text{sMoS}_2$ . Fe foil, hydrated  $\text{FeCl}_2$ , and  $\text{FeCl}_3$  were used as references. (c) Wavelet transformation for the  $k^2$ -weighted Fe K-edge XAFS signals of Fe- $\text{sMoS}_2$  and Fe foil based on Morlet wavelets with optimum resolutions at the first and higher coordination shells. The intensity reflects the content of scattering signals. Intensity decreases in order of red, yellow, green, and blue.



**Fig. 3**  $\text{N}_2$  reduction in aqueous solution and relationship between activity and structure. (a)  $\text{N}_2$  reduction activity to  $\text{NH}_3$  over Fe-sMoS<sub>2</sub> under applied potentials in the range of  $-0.05$  V to  $-1.00$  V. Activity was evaluated at least 3 times under the same conditions to generate the measurement errors for the ammonia production rate ( $R_{\text{NH}_3}$ ) and faradaic efficiency ( $\eta_{\text{FE}}$ ). (b) Linear sweep voltammetry from  $0.10$  V to  $-0.50$  V versus RHE over Fe-sMoS<sub>2</sub> under Ar and  $\text{N}_2$ .  $\text{N}_2$  reduction efficiency for  $\text{NH}_3$  production at different applied potentials was extrapolated from the linear sweep voltammetry curves. The  $\text{NH}_3$  yield is expressed as  $\mu\text{g cm}^{-2}\text{h}^{-1}$  ( $\mu\text{g}_{\text{NH}_3}$  per centimeter square of electrode per hour). (c) Calculated amount of electrons consumed for the nitrogen reduction reaction (NRR) and hydrogen evolution reaction (HER) at  $-0.1$  V in 1 h over [M-S<sub>2</sub>-Mo] (M represents metal as shown in x-axis) dwelling in single-layered MoS<sub>2</sub> assuming no heat was generated from the current. (d) Electron paramagnetic resonance spectra of over different thickness MoS<sub>2</sub> samples and transition metals.

reported results for the electrochemical synthesis of  $\text{NH}_3$  using non-noble Fe-based systems in the literature (Table S2†). However, both the rate and  $\eta_{\text{FE}}$  decreased dramatically when the applied potential was beyond  $-0.20$  V (Fig. 3b). The Tafel plot in Fig. S11† was used to determine the rate-determining step for the  $\text{H}_2$  evolution reaction and oxygen reduction reaction. Mechanistically, three principal steps can participate in the conversion of  $2\text{H}^+$  to  $\text{H}_2$ , namely the Volmer, Heyrovsky and Tafel steps. If the Volmer process is the rate-determining step (rds), a slope of  $\sim 120$  mV per decade will likely be obtained. In contrast, a rate-determining Heyrovsky or Tafel step gives characteristic slopes between  $30$ – $40$  mV per decade.<sup>40</sup> Our Tafel slope for Fe-sMoS<sub>2</sub> in argon gas was measured to be  $\sim 156$  mV per decade at a low over-potential range (Fig. S11†), which suggests the rds is the Volmer step, involving the initial highly activated adsorption and reduction of  $\text{H}^+$  to produce active surface  $\text{H}^*$  ( $\text{H}^+ + \text{e}^- + * = *\text{H}$ ). On the other hand, the corresponding Tafel slope for Fe-sMoS<sub>2</sub> for  $\text{N}_2$  reduction to ammonia was measured to be  $\sim 121$  mV per decade, which is substantially lower than that of the proton reduction. Therefore, to reduce the extent of  $\text{H}_2$  production on this surface during  $\text{N}_2$  reduction, it appears to be necessary to apply an optimal potential.

It is well known that exposed lattice vacancies can act as active sites for the activation of  $\text{H}_2$  and  $\text{N}_2$ .<sup>41–43</sup> Consequently, different concentrations of S vacancies in different-layered MoS<sub>2</sub> samples using electron paramagnetic resonance were obtained (EPR, Fig. 3d). As can be seen in Fig. 3d, the peak

intensity due to S vacancies (unpaired electrons at  $g = 2.00$  detected infer the formation of S vacancies) increased with S decrease in the thickness of the MoS<sub>2</sub> layers (S vacancies were created during exfoliation<sup>25</sup>), which correlates well with their electrochemical performances at a potential of  $-0.1$  V (versus RHE, Fig. 3d and S12†). The activity for both  $\text{N}_2$  reduction and  $\text{H}_2$  evolution appeared to be greatly promoted when single-layered MoS<sub>2</sub> was used. Notably, the activity for  $\text{NH}_3$  yield apparently increased with a reduction in the thickness of the MoS<sub>2</sub> slab. However, the overall  $\eta_{\text{FE}}$  for  $\text{N}_2$  reduction to  $\text{NH}_3$  by the single-layered MoS<sub>2</sub> was significantly lower than that of few-layered MoS<sub>2</sub> and bulk MoS<sub>2</sub>. This implies that S vacancies promote a greater degree of  $\text{H}_2$  evolution than  $\text{N}_2$  reduction due to the more favorable thermodynamics in the former case. The addition of a transition metal causes an obvious decrease in the EPR signal, presumably because the transition metal dopant can occupy the S vacancies of 2H-MoS<sub>2</sub>, as shown by the HAADF-STEM analysis (Fig. 1c). Fe-sMoS<sub>2</sub> exerts strong magnetic perturbation due to the presence of paramagnetic Fe, which accounts for the perturbed zig-zag oscillation of the background ESR signal. Fig. S13† shows a comparison of the activities and  $\eta_{\text{FE}}$  for  $\text{N}_2$  reduction to  $\text{NH}_3$  over different metal-doped sMoS<sub>2</sub> such as Au and Ru with the previously reported values.<sup>44,45</sup> The presence of trace  $\text{Li}^+$  during the preparation of the molecular layer of MoS<sub>2</sub> may facilitate the activity and  $\eta_{\text{FE}}$  since  $\text{Li}^+$  has been reported to play a vital role in the NRR.<sup>46</sup> However, the result from Fig. S13† indicates that the metal doping affects much more than the residual  $\text{Li}^+$ . Polarization due to protruded transition metal atoms on the thin MoS<sub>2</sub> surface suggested by L. Zhang and co-workers may play a role in their activity.<sup>47</sup> However, we believe that the intrinsic atomic arrangements of Fe-sMoS<sub>2</sub>, which has the core structure of nitrogenase, can give the best activity and  $\eta_{\text{FE}}$ . In fact, among the Haber-Bosch catalysts and biological enzymes, Fe is well-known to bind N and H competitively to give ammonia compared to other metals. This is further supported by the high electron consumption for the nitrogen reduction reaction over Fe-sMoS<sub>2</sub>, as shown in Fig. 3c.

The electrochemical performance for  $\text{N}_2$  fixation to  $\text{NH}_3$  on Fe-sMoS<sub>2</sub> was also studied by linear sweep voltammetry (LSV). As shown in Fig. 3b, a clearly higher cathodic current density can be observed in the sweeping potential range of  $-50$  mV to  $-300$  mV versus RHE when the electrolyte was purged with  $\text{N}_2$  instead of Ar. In addition, the  $\eta_{\text{FE}}$  for  $\text{N}_2$  reduction by dividing the current density in Ar is very close to that in the synthesis of  $\text{NH}_3$  (maximum of 27%), verifying that  $\text{N}_2$  is activated and converted to  $\text{NH}_3$  by the Fe-sMoS<sub>2</sub> catalyst. Isotopic labeling using 98% <sup>15</sup>N-enriched  $\text{N}_2$  gas was carried out to prove the derivation of  $\text{NH}_3$ . Controlled experiments in the absence of <sup>15</sup>N<sub>2</sub>, catalyst, and applied potential were firstly conducted, and no clear ammonia signal was observed in the proton NMR spectra, as shown in Fig. S14.† In contrast, a doublet in the region near 7.0 ppm was found for the test over Fe-sMoS<sub>2</sub> at  $-0.10$  V with a flow of <sup>15</sup>N<sub>2</sub>. The quantitative results (Fig. S15†) indicated that the product rate is around  $22 \mu\text{g cm}^{-2}\text{h}^{-1}$ , which is consistent with the result using <sup>14</sup>N<sub>2</sub>. These results show that both the catalyst and the applied potential are necessary for

nitrogen fixation. Thus, based on the result from LSV, nitrogen fixation occurs at a potential in the range of 0 to  $-0.5$  V. Subsequently, liquid chromatography-mass spectrometry (LC-MS) analysis was conducted, which identified two major species containing indophenol derivatives from natural  $^{14}\text{N}$  and enriched  $^{15}\text{N}$  (see Fig. S16†).<sup>17,48</sup> The fragments containing  $^{15}\text{N}$  have a much higher area ratio at  $199/198\text{ }m/z$  (mass/charge ratio) compared to that of the control fragments containing  $^{14}\text{N}$ . The isotopically labeled  $^{15}\text{N}_2$  authenticated that the  $\text{NH}_3$  synthesized originated from  $\text{N}_2$  reduction. These results gave sufficient proof that  $\text{N}_2$  can be fixed to  $\text{NH}_3$  over Fe-s $\text{MoS}_2$ . We conducted a 10 h chronoamperometry test, which demonstrated that the activity and  $\eta_{\text{FE}}$  slightly changed, as shown in Fig. S17†.

### Molecular activation and reduction of $\text{N}_2$

*Operando* Fe K-edge opXAFS and opXANES are sensitive techniques to monitor the chemical environment of Fe atoms, which were performed in this study at the B18 Beamline, Diamond Light Source, UK to study the structural dynamics involving the single Fe atoms upon the competitive adsorption and activation of  $\text{N}_2$  with a proton from water over Fe-s $\text{MoS}_2$ . Fig. 4a and c show the Fourier transform (FT) opEXAFS spectra

and the corresponding Fe K-edge opXANES spectra under different experimental conditions. Particularly, the peak relative to the Fe-S bond attributed to the Mo atop site (see Fig. 3a) under open-circuit voltage is compared in  $\text{N}_2$ ,  $\text{Ar}/\text{H}_2\text{O}$ , and  $\text{N}_2/\text{H}_2\text{O}$ , and at  $-0.1$  V (*versus* RHE) in  $\text{N}_2/\text{H}_2\text{O}$ . It is clear that the FT intensity near the Fe-S bonds at the Mo atop site clearly changes in this region to the different treatments. After switching to highly acidic electrolyte solution purged with Ar, the intensity of the Fe-S peak attributed to the Fe atop site exhibited the lowest value, which indicates the lowest coordination number for this Fe species. Based on our DFT simulation, the Fe-N bonding interactions of these molecule-absorbed Fe-s $\text{MoS}_2$  species are at around  $1.8$  Å (Fig. S18†), which is comparable in distance with the Fe-S interactions. Thus, it was anticipated that competitive replacement of this absorbed  $\text{N}_2$  species from Fe by  $\text{H}^+$  would cause a reduction in the intensity of this peak. Interestingly, upon switching the gas stream back to  $\text{N}_2$ , we noted that the peak intensity increased to a higher value, resuming the higher contribution from the Fe-N scattering. These results clearly show that  $\text{N}_2$  and  $\text{H}^+$  can be competitively activated by the  $\text{Fe}_1$  atoms on  $\text{MoS}_2$ , as reflected by the atop Fe-S peak modulations. During the typical conditions for electrochemical  $\text{N}_2$  reduction to  $\text{NH}_3$  at the previously optimized  $-0.1$  V *versus* RHE, the

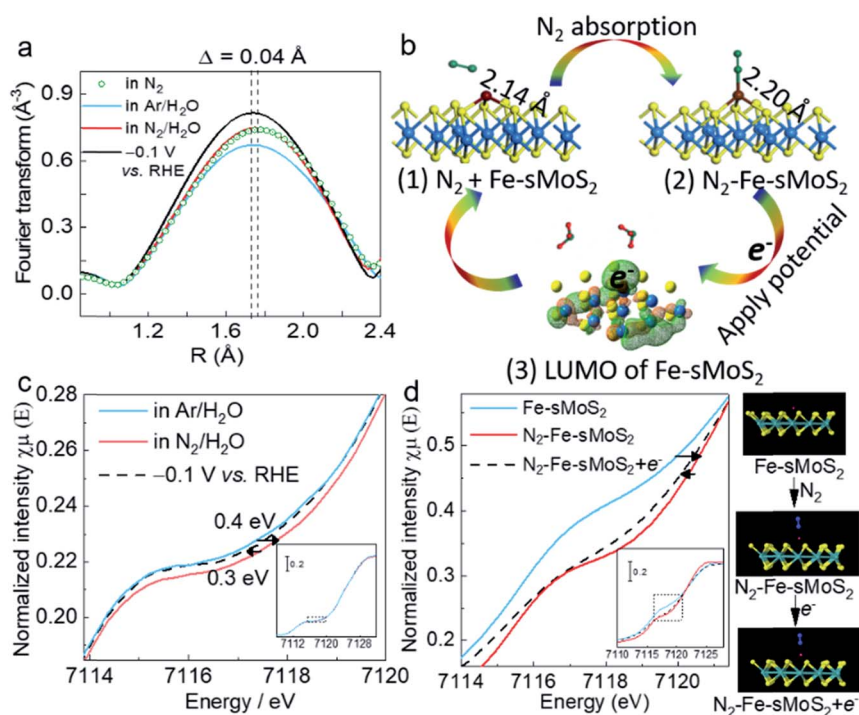


Fig. 4 Operando X-ray absorption spectroscopy and  $\text{N}_2$  activation process. (a) Fourier transform magnitudes of the experimental Fe K-edge srXAFS spectra of Fe-s $\text{MoS}_2$  under open-circuit voltage bias in  $\text{N}_2$ ,  $\text{Ar}/\text{H}_2\text{O}$ , and  $\text{N}_2/\text{H}_2\text{O}$ , and at  $-0.1$  V (*versus* RHE) in  $\text{N}_2/\text{H}_2\text{O}$ .  $\text{H}_2\text{O}$  represents electrolyte solution containing  $0.1\text{ M}$  hydrogen chloride. (b) Structural evolution of the active site in electrochemical  $\text{NH}_3$  synthesis with  $\text{N}_2$  absorption and applied potential. (1) Before  $\text{N}_2$  adsorption, the Fe-S bond is  $2.14$  Å in length. (2) After the adsorption of  $\text{N}_2$  on the  $\text{Fe}_1$  atom, the Fe-S bond is extended to  $2.20$  Å in length. (3) Low unoccupied molecular orbital of  $\text{Fe}_1$  Mo atop site. Green net represents positively charged orbital and orange net represents negatively charged orbital. After applying a potential, the electron will transfer to the  $\text{Fe}_1$  atom. Blue, yellow, brown, green, and red balls are Mo, S, Fe, N, and H atoms, respectively. (c) Normalized *operando* Fe K-edge XANES spectra for Fe-s $\text{MoS}_2$  under open-circuit voltage bias in  $\text{Ar}/\text{H}_2\text{O}$ , and  $\text{N}_2/\text{H}_2\text{O}$ , and at  $-0.1$  V (*versus* RHE) in  $\text{N}_2/\text{H}_2\text{O}$ . (d) Simulated Fe K-edge XANES spectra for Fe-s $\text{MoS}_2$ ,  $\text{N}_2$ -adsorbed Fe-s $\text{MoS}_2$ , and  $\text{N}_2$ -adsorbed Fe-s $\text{MoS}_2$  with electron-rich Fe. Blue, yellow, brown, cyan, and red balls are N, S, Fe, and Mo atoms, respectively.

intensity of opXAFS was significantly enhanced, which implies that the dynamic  $\text{N}_2$  adsorption to  $\text{NH}_3$  was greatly strengthened, corresponding to the same phenomenon observed in Fig. 3a. This also indicates that the electron from the applied potential is biased at the  $\text{Fe}_1$  atom and could be used for competitive  $\text{N}_2$  activation to  $\text{NH}_3$ . In addition, the Fourier transform spectra showed that there was a slight but significant shift in the Fe–S interaction of the atop site during  $\text{N}_2$  activation, as shown in Fig. 4a. The main peak of Fe–S shifted to a shorter length ( $\sim \Delta 0.04 \text{ \AA}$ ) upon switching to Ar flushing and returned to the original position when the  $\text{N}_2$  flow was resumed. Clearly, the electron back-donation of Fe orbitals from the adsorbed  $\text{N}_2$  can attenuate its bonding with the S ligands, accounting for the longer Fe–S interaction. Apparently, applying a negative over-potential for  $\text{N}_2$  over  $\text{H}^+$  in the dynamic synthesis of ammonia places the peak position between these two values.

The processes for  $\text{N}_2$  activation were then investigated by DFT calculations (Fig. S19†). Fig. 4b(1) shows that the DFT-optimised Fe–S bond of the initial  $\text{Fe}_1$  atom at the Mo atop site is  $2.14 \text{ \AA}$ . After the absorption of  $\text{N}_2$ , the bond is extended by absorbed  $\text{N}_2$  to  $2.20 \text{ \AA}$  (Fig. 4c(2)). The increment in the bond length ( $\sim 0.06 \text{ \AA}$ ) is close to the observed value ( $\sim 0.04 \text{ \AA}$ ), as measured by opXAFS. The electron ground state of  $\text{Fe-sMoS}_2$  was simulated in the form of the highest occupied molecular orbital (HOMO). As shown in Fig. 4c(3),  $\text{Fe}_1$  is relatively positively charged under  $\text{N}_2$ , which allows the external electrons to occupy it under HOMO excitation. The experimental result from opXAFS also confirmed that the external electrons from the applied potential will be accommodated at the  $\text{Fe}_1$  atom, as above. Therefore, the electron can then be used for the activation and reduction of  $\text{N}_2$  to  $\text{NH}_3$  on [Fe–S<sub>2</sub>–Mo].

Fig. 4c shows the corresponding normalized *operando* Fe K-edge opXANES spectra in Ar. The shoulder signal of the main absorption edge at  $\sim 7118 \text{ eV}$  is due to the  $1s \rightarrow 4p$  transition. The introduction of  $\text{N}_2$  caused a shift to the right, showing an electron withdrawing effect from the Fe species to  $\text{N}_2$ , indicating the electronic effects on the  $\text{Fe}_1$  atom *via*  $\text{N}_2$  adsorption. The shift to a higher oxidative state is due to the effective delocalization of the unpaired electron in the 3d orbitals of Fe and the spontaneous charge transfer from Fe to both the  $\text{N}_2$  2p orbital and proton 1s orbital. During electrochemical  $\text{N}_2$  reduction, the Fe K-edge of  $\text{Fe-sMoS}_2$  shifted back to a lower shift value, indicating the recovery of the electronic state of the orbitals of  $\text{Fe}_1$  due to the injection of external electrons. We further monitored this process using XANES simulations for  $\text{Fe-sMoS}_2$  under different conditions (Fig. 4d). As shown, the  $\text{N}_2$  adsorption on the  $\text{Fe}_1$  atom significantly shifted the edge of  $1s \rightarrow 4p$  transition, which returned to a lower energy value after applying one electron to the Fe atom. The simulations confirmed the trend of the effect of  $\text{N}_2$  activation and potential applied. Similar phenomena of opXAFS and opXANES were observed for the molecular activation and reduction of  $\text{CO}_2$ .<sup>49</sup>

Thus, based on these *operando* studies, the  $\text{Fe}_1$  single atom on  $\text{Fe-sMoS}_2$  serves as the active site for the electrochemical fixation of  $\text{N}_2$  to  $\text{NH}_3$ . During the adsorption and electrochemical reduction of  $\text{N}_2$ , [Fe–S<sub>2</sub>–Mo] responds to the tension

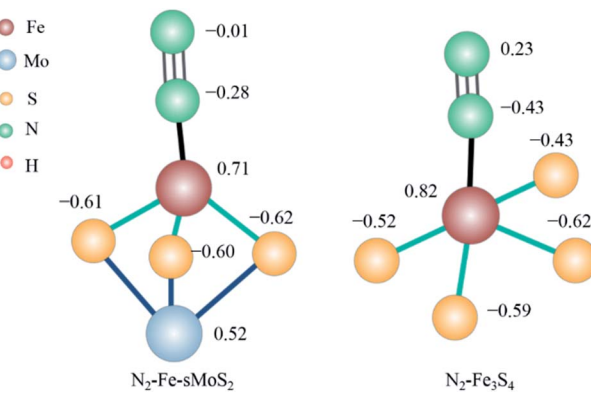


Fig. 5 Electronic structure of  $\text{N}_2$  activation over nitrogenase-mimic  $\text{Fe-sMoS}_2$  and  $\text{Fe}_3\text{S}_4$ . The presented data is the Bader charge of the corresponding atoms in units of electrons.

and contraction of the Fe–S bond by changing the bond length and Fe electronic state.

To demonstrate the electron-mediating and catalytic roles of the [Fe–S<sub>2</sub>–Mo] unit in promoting the synthesis of ammonia, we compared the electronic structure of  $\text{N}_2\text{-Fe-sMoS}_2$  and  $\text{N}_2\text{-Fe}_3\text{S}_4$ . As shown in Fig. 5, the Bader charge of adsorbed  $\text{N}_2$  is  $-0.29$  electrons ( $-0.01\text{--}0.28$ ) over  $\text{Fe-sMoS}_2$ . This value is much lower than that ( $0.23\text{--}0.43 = -0.20$  electrons) over  $\text{Fe}_3\text{S}_4$ , indicating that more electrons are donated from the  $\text{Fe}_1$  site to the antibonding orbital of the adsorbed  $\text{N}_2$  on  $\text{Fe-sMoS}_2$  with [Fe–S<sub>2</sub>–Mo] units than  $\text{Fe}_3\text{S}_4$  without Mo. Consequently, the activation of  $\text{N}_2$  is promoted with a longer N–N bond length from  $1.10 \text{ \AA}$  to  $1.15 \text{ \AA}$  (see Table S3†). Meanwhile, the bond length of Fe–N is shortened within the unit of [Fe–S<sub>2</sub>–Mo]. In addition, the average Bader charge of the S atom in the [Fe–S<sub>2</sub>–Mo] unit is also more negative than that without the nitrogenase-mimic structure ( $-0.61$  vs.  $-0.54$  electrons), indicating that the removal of a proton from the competitive active site of the Fe atom is easier for a higher efficiency of nitrogen reduction over the nitrogenase mimic  $\text{Fe-sMoS}_2$  under the same potential.

## Conclusions

In summary, a new inorganic-based electrocatalyst with  $\text{Fe}_1$  on a 2D single-layer  $\text{MoS}_2$  slab was described. The structure contained dispersed Fe atoms on nitrogenase-like [Fe–S<sub>2</sub>–Mo] motifs, which showed superior electrochemical activity and  $\eta_{\text{FE}}$  for electrochemical  $\text{N}_2$  fixation to  $\text{NH}_3$  over proton reduction in water under the application of the optimal potential at  $0.1 \text{ V}$ . *Operando* Fe K-edge srXAFS, XANES and DFT calculations indicated that  $\text{N}_2$  can be adsorbed and reduced at the catalytic  $\text{Fe}_1$  site on the essential electron-mediating [Fe–S<sub>2</sub>–Mo] motifs. To activate the  $\text{N}_2$  molecule, the strain of the Fe–S bonds and redox states of the  $\text{Fe}_1$  atom will adapt to accelerate the absorption and reduction processes. This work not only demonstrated that single-atom heterogeneous catalysis accelerates the electrochemical reduction of  $\text{N}_2$ , but also offers unique insight into the synergistic active site with electronic

and structural transitions during N<sub>2</sub> fixation over the nitrogenase mimic [Fe-S<sub>2</sub>-Mo] structure.

## Conflicts of interest

The authors declare no competing financial interest.

## Acknowledgements

The support of this project from the IUK-EPSRC of UK (DGE 102000) is gratefully acknowledged. The authors wish to thank Diamond Light Source (Diamond, UK) for accessing STEM and XAS facilities (B18; SP20856-1). LL also acknowledges the use of the Computing Facilities of Wuhan University of Science and Technology in the completion of the theoretical part of this work.

## Notes and references

- 1 J. G. Chen, R. M. Crooks, L. C. Seefeldt, K. L. Bren, R. M. Bullock, M. Y. Daresbourg, P. L. Holland, B. Hoffman, M. J. Janik, A. K. Jones and M. G. Kanatzidis, *Science*, 2018, **360**, eaar6611.
- 2 E. Worrell, L. Price, M. Neelis, C. Galitsky and Z. Nan, *World best practice energy intensity values for selected industrial sectors*, Tech. Rep., LBNL-62806 Ernest Orlando Lawrence Berkeley National Laboratory, 2008.
- 3 D. Tilman, K. G. Cassman, P. A. Matson, R. Naylor and S. Polasky, *Nature*, 2002, **418**, 671–677.
- 4 H. Wang, L. Wang, Q. Wang, S. Ye, W. Sun, Y. Shao, Z. Jiang, Q. Qiao, Y. Zhu, P. Song and D. Li, *Angew. Chem., Int. Ed.*, 2018, **57**, 12360–12364.
- 5 H. Li, J. Shang, Z. Ai and L. Zhang, *J. Am. Chem. Soc.*, 2015, **137**, 6393–6399.
- 6 L. Ye, R. Nayak-Luke, R. Banares-Alcantara and E. Tsang, *Chem*, 2017, **3**, 712–714.
- 7 J. Zheng, F. Liao, S. Wu, G. Jones, T. Y. Chen, J. Fellowes, T. Sudmeier, I. J. McPherson, I. Wilkinson and S. C. E. Tsang, *Angew. Chem., Int. Ed.*, 2019, **58**, 17335–17341.
- 8 S. Chen, S. Perathoner, C. Ampelli, C. Mebrahtu, D. Su and G. Centi, *Angew. Chem., Int. Ed.*, 2017, **56**, 2699–2703.
- 9 R. D. Milton, R. Cai, S. Sahin, S. Abdellaoui, B. Alkotaini, D. N. Leech and S. D. Minteer, *J. Am. Chem. Soc.*, 2017, **139**, 9044–9052.
- 10 H. Hirakawa, M. Hashimoto, Y. Shiraishi and T. Hirai, *J. Am. Chem. Soc.*, 2017, **139**, 10929–10936.
- 11 H. Tao, C. Choi, L. X. Ding, J. Zheng, Z. Han, M. Jia, Q. Fan, Y. Gao, H. Wang, A. W. Robertson, S. Hong, Y. Jung, S. Liu and Z. Sun, *Chem*, 2019, **5**, 204–214.
- 12 E. J. Vicente and D. Dean, *Proc. Natl. Acad. Sci. U. S. A.*, 2017, **114**, 3009–3011.
- 13 B. M. Hoffman, D. Lukoyanov, Z.-Y. Yang, D. R. Dean and L. C. Seefeldt, *Chem. Rev.*, 2014, **114**, 4041–4062.
- 14 T. Kandemir, M. E. Schuster, A. Senyshyn, M. Behrens and R. Schlögl, *Angew. Chem., Int. Ed.*, 2013, **52**, 12723–12726.
- 15 M. J. Chalkley, T. J. Del Castillo, B. D. Matson, J. P. Roddy and J. C. Peters, *ACS Cent. Sci.*, 2017, **3**, 217–223.
- 16 J. S. Anderson, J. Rittle and J. C. Peters, *Nature*, 2013, **501**, 84–87.
- 17 A. Banerjee, B. D. Yuhas, E. A. Margulies, Y. Zhang, Y. Shim, M. R. Wasielewski and M. G. Kanatzidis, *J. Am. Chem. Soc.*, 2015, **137**, 2030–2034.
- 18 J. Liu, M. S. Kelley, W. Wu, A. Banerjee, A. P. Douvalis, J. Wu, Y. Zhang, G. C. Schatz and M. G. Kanatzidis, *Proc. Natl. Acad. Sci. U. S. A.*, 2016, **113**, 5530–5535.
- 19 B. M. Lindley, A. M. Appel, K. Krogh-Jespersen, J. M. Mayer and A. J. Miller, *ACS Energy Lett.*, 2016, **1**, 698–704.
- 20 D. R. Cummins, U. Martinez, A. Sherehiy, R. Kappera, A. Martinez-Garcia, R. K. Schulze, J. Jasinski, J. Zhang, R. K. Gupta and J. Lou, *Nat. Commun.*, 2016, **7**, 11857.
- 21 J. H. Montoya, C. Tsai, A. Vojvodic and J. K. Nørskov, *ChemSusChem*, 2015, **8**, 2180–2186.
- 22 C. J. Jacobsen, S. Dahl, B. S. Clausen, S. Bahn, A. Logadottir and J. K. Nørskov, *J. Am. Chem. Soc.*, 2001, **123**, 8404–8405.
- 23 K. M. Lancaster, M. Roemelt, P. Ettenhuber, Y. Hu, M. W. Ribbe, F. Neese, U. Bergmann and S. DeBeer, *Science*, 2011, **334**, 974–977.
- 24 J. Chen, J. Christiansen, N. Campobasso, J. T. Bolin, R. C. Tittsworth, B. J. Hales, J. J. Rehr and S. P. Cramer, *Angew. Chem., Int. Ed.*, 1993, **32**, 1592–1594.
- 25 G. Liu, A. W. Robertson, M. M. Li, W. C. Kuo, M. T. Darby, M. H. Muhieddine, Y. C. Lin, K. Suenaga, M. Stamatakis, J. H. Warner and S. C. E. Tsang, *Nat. Chem.*, 2017, **9**, 810–816.
- 26 H. Fei, J. Dong, M. J. Arellano-Jimenez, G. Ye, N. D. Kim, E. L. Samuel, Z. Peng, Z. Zhu, F. Qin, J. Bao and M. J. Yacaman, *Nat. Commun.*, 2015, **6**, 8668.
- 27 R. Bjornsson, F. Neese, R. R. Schrock, O. Einsle and S. DeBeer, *J. Biol. Inorg. Chem.*, 2015, **20**, 447–460.
- 28 R. Bjornsson, F. A. Lima, T. Spatzal, T. Weyhermüller, P. Glatzel, E. Bill, O. Einsle, F. Neese and S. DeBeer, *Chem. Sci.*, 2014, **5**, 3096–3103.
- 29 A. Kropf, B. Bunker, M. Eisner, S. Moss, L. Zecca, A. Stroppolo and P. Crippa, *Biophys. J.*, 1998, **75**, 3135–3142.
- 30 J. Jakob, J. K. Norskov and I. Chorkendorff, *ACS Energy Lett.*, 2019, **4**, 2986–2988.
- 31 J. Long, S. Chen, Y. Zhang, C. Guo, X. Fu, D. Deng and J. Xiao, *Angew. Chem., Int. Ed.*, 2020, **59**, 9711–9718.
- 32 A. Pourmohammaghader, E. Jamshidi, H. Ale-Ebrahim and S. Dabir, *Ind. Eng. Chem. Res.*, 2011, **50**, 8278–8284.
- 33 C. Brogren, H. T. Karlsson and I. Bjerle, *Chem. Eng. Technol.*, 1998, **21**, 61–70.
- 34 B. R. Deshwal, D. S. Jin, S. H. Lee, S. H. Moon, J. H. Jung and H. K. Lee, *J. Hazard. Mater.*, 2008, **150**, 649–655.
- 35 J. Choi, H. L. Du, C. K. Nguyen, B. H. Suryanto, A. N. Simonov and D. R. MacFarlane, *ACS Energy Lett.*, 2020, **5**, 2095–2097.
- 36 L. F. Greenlee, J. N. Renner and S. L. Foster, *ACS Catal.*, 2018, **8**, 7820–7827.
- 37 S. Z. Andersen, V. Colic, S. Yang, J. A. Schwalbe, A. C. Nielander, J. M. McEnaney, K. Enemark-Rasmussen, J. G. Baker, A. R. Singh, B. A. Rohr, M. J. Statt, S. J. Blair, S. Mezzavilla, J. Kibsgaard, P. C. K. Vesborg, M. Cargnello, S. F. Bent, T. F. Jaramillo, I. E. L. Stephens, J. K. Norskov and I. Chorkendorff, *Nature*, 2019, **570**, 504–508.
- 38 C. Tang and S. Z. Qiao, *Chem. Soc. Rev.*, 2019, **48**, 3166–3180.

- 39 Y. Ma, T. Yang, H. Zou, W. Zang, Z. Kou, L. Mao, Y. Feng, L. Shen, S. J. Pennycook, L. Duan, X. Li and J. Wang, *Adv. Mater.*, 2020, 2002177.
- 40 T. Shinagawa, A. T. Garcia-Esparza and K. Takanabe, *Sci. Rep.*, 2015, 5, 13801.
- 41 T. Wu, Z. Xing, S. Mou, C. Li, Y. Qiao, Q. Liu, X. Zhu, Y. Luo, X. Shi and Y. Zhang, *Angew. Chem., Int. Ed.*, 2019, 58, 18449–18453.
- 42 C. Lv, Y. Qian, C. Yan, Y. Ding, Y. Liu, G. Chen and G. Yu, *Angew. Chem., Int. Ed.*, 2018, 57, 10246–10250.
- 43 H. Li, C. Tsai, A. L. Koh, L. Cai, A. W. Contryman, A. H. Fragapane, J. Zhao, H. S. Han, H. C. Manoharan and F. Abild-Pedersen, *Nat. Mater.*, 2016, 15, 48–53.
- 44 S. J. Li, D. Bao, M. M. Shi, B. R. Wulan, J. M. Yan and Q. Jiang, *Adv. Mater.*, 2017, 29, 1606550.
- 45 B. H. Suryanto, D. Wang, L. M. Azofra, M. Harb, L. Cavallo, R. Jalili, D. R. G. Mitchell, M. Chatti and D. R. MacFarlane, *ACS Energy Lett.*, 2018, 4, 430–435.
- 46 G.-F. Chen, X. Cao, S. Wu, X. Zeng, L.-X. Ding, M. Zhu and H. Wang, *J. Am. Chem. Soc.*, 2017, 139, 9771–9774.
- 47 J. Li, S. Chen, F. Quan, G. Zhan, F. Jia, Z. Ai and L. Zhang, *Chem.*, 2020, 6, 808–810.
- 48 Y. Zhao, Y. Zhao, R. Shi, B. Wang, G. I. Waterhouse, L. Z. Wu, C. H. Tung and T. Zhang, *Adv. Mater.*, 2019, 31, 1806482.
- 49 H. B. Yang, S.-F. Hung, S. Liu, K. Yuan, S. Miao, L. Zhang, X. Huang, H.-Y. Wang, W. Cai and R. Chen, *Nat. Energy*, 2018, 3, 140–147.